



## NRC Publications Archive Archives des publications du CNRC

### **Growth and characterization of metastable hexagonal nickel thin films via plasma-enhanced atomic layer deposition**

Motamedi, Pouyan; Bosnick, Ken; Cui, Kai; Cadien, Ken; Hogan, James  
David

This publication could be one of several versions: author's original, accepted manuscript or the publisher's version. /  
La version de cette publication peut être l'une des suivantes : la version prépublication de l'auteur, la version  
acceptée du manuscrit ou la version de l'éditeur.

For the publisher's version, please access the DOI link below. / Pour consulter la version de l'éditeur, utilisez le lien  
DOI ci-dessous.

#### **Publisher's version / Version de l'éditeur:**

<https://doi.org/10.1021/acsami.7b05571>

*ACS Applied Materials & Interfaces*, 9, 29, pp. 24722-24730, 2017-07-03

#### **NRC Publications Record / Notice d'Archives des publications de CNRC:**

<https://nrc-publications.canada.ca/eng/view/object/?id=82479cdb-9a3f-44b4-88f0-24c6dd0f3e62>

<https://publications-cnrc.canada.ca/fra/voir/objet/?id=82479cdb-9a3f-44b4-88f0-24c6dd0f3e62>

Access and use of this website and the material on it are subject to the Terms and Conditions set forth at

<https://nrc-publications.canada.ca/eng/copyright>

READ THESE TERMS AND CONDITIONS CAREFULLY BEFORE USING THIS WEBSITE.

L'accès à ce site Web et l'utilisation de son contenu sont assujettis aux conditions présentées dans le site

<https://publications-cnrc.canada.ca/fra/droits>

LISEZ CES CONDITIONS ATTENTIVEMENT AVANT D'UTILISER CE SITE WEB.

#### **Questions?** Contact the NRC Publications Archive team at

PublicationsArchive-ArchivesPublications@nrc-cnrc.gc.ca. If you wish to email the authors directly, please see the  
first page of the publication for their contact information.

**Vous avez des questions?** Nous pouvons vous aider. Pour communiquer directement avec un auteur, consultez la  
première page de la revue dans laquelle son article a été publié afin de trouver ses coordonnées. Si vous n'arrivez  
pas à les repérer, communiquez avec nous à PublicationsArchive-ArchivesPublications@nrc-cnrc.gc.ca.



National Research  
Council Canada

Conseil national de  
recherches Canada

Canada

# Growth and Characterization of Metastable Hexagonal Nickel Thin Films via Plasma-Enhanced Atomic Layer Deposition

Pouyan Motamedi,<sup>\*,†,§</sup> Ken Bosnick,<sup>†</sup> Kai Cui,<sup>†</sup> Ken Cadien,<sup>‡</sup> and James David Hogan<sup>§</sup>

<sup>†</sup>National Research Council Canada – National Institute for Nanotechnology, 11421 Saskatchewan Drive, Edmonton, AB T6G 2M9, Canada

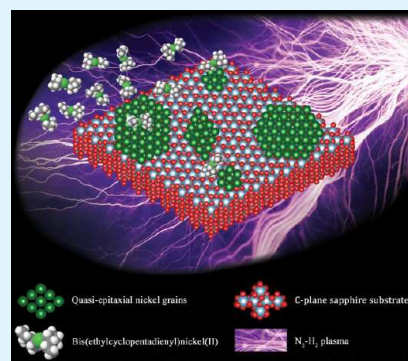
<sup>‡</sup>Department of Chemical and Materials Engineering, University of Alberta, 9211–116 St., Edmonton, AB T6G 2G6, Canada

<sup>§</sup>Department of Mechanical Engineering, University of Alberta, 9211–116 St., Edmonton, AB T6G 2R3, Canada

## S Supporting Information

**ABSTRACT:** There is a great interest in various branches of the advanced materials industry for the development of novel methods (and improvements to existing ones) for the deposition of conformal ultrathin metallic films. In most of these applications, like enhanced solar absorbers and microelectronics, achieving the capacity to deposit a conformal thin film on a three-dimensional structure is an important condition. Plasma-enhanced atomic layer deposition (ALD) is known for its potential for growth of conformal thin films with a precise control over the thickness and its capability for deposition at relatively low temperatures (below 500 °C). This study evaluates the potential of plasma-enhanced ALD for growth of conformal nickel thin films, using bis(ethylcyclopentadienyl)nickel and nitrogen/hydrogen plasma as precursors. A comprehensive analysis of the structure, composition, and physical properties of the films was performed. The results indicate that conformal nickel films with low levels of impurity were successfully deposited on sapphire. The films had a roughness of  $R_a = 1.5$  nm and were seen to be under strain. The deposited nickel had a hexagonal crystal structure, with a random in-plane orientation of the grains, while the grains had their *c*-axes oriented along the normal to the interface. These results pave the way for conformal low-temperature deposition of high-quality nickel thin films on three-dimensional structures.

**KEYWORDS:** nickel, atomic layer deposition, hexagonal, HCP, XRD, TEM, AFM



## 1. INTRODUCTION

Ultrathin metallic films are emerging as an increasingly important subject of interest in the advanced electronics industry. High conductivity and flexibility, among other physical and mechanical properties, make these materials suitable candidates for numerous applications, such as transparent electrodes,<sup>1–4</sup> enhanced solar absorbers,<sup>5</sup> microelectronics,<sup>6,7</sup> and bioanalysis devices.<sup>8</sup> Specific types of ultrathin metallic films can act as efficient catalysts for the deposition of carbon nanotubes, as reported earlier by Bosnick et al.<sup>9</sup>

The successful deposition of ultrathin metal films for such applications is contingent upon meeting a few key conditions. It is well-known that several electrical<sup>10,11</sup> and optical<sup>12,13</sup> properties of thin films vary with thickness. Therefore, precise thickness control is one crucial requirement, when a desirable level of command over physical properties is to be realized. In addition, the ability to deposit thin films conformally over substrates with high aspect ratios will be a key advantage for most of the applications, as deposition on the three-dimensional structures is often required. Self-saturating non-directional growth methods are favored for this purpose. Another important characteristic of ultrathin films is the fact that they lack the sufficient thickness to allow for relaxation of interfacial strain.<sup>1</sup> Since the difference in the coefficient of

thermal expansion between the film and the substrate is a major element that gives rise to this strain, deposition at low temperatures will be beneficial.<sup>14</sup>

A comparison of the commercially available deposition methods, such as ion beam sputtering, chemical vapor deposition, molecular beam epitaxy, and electron beam evaporation reveals that all these methods partially fail at meeting the previously mentioned requirements, i.e., low-temperature capability, conformality, and precise thickness control. Plasma-enhanced atomic layer deposition (PEALD), however, is well suited for growth of conformal ultrathin metal films with precisely controlled thickness at relatively low growth temperatures.<sup>15,16</sup> Importantly, applying ALD for synthesis of very thin films effectively nullifies the major drawback associated with this method, i.e., a relatively long growth time.

Among several different metals, whose deposition via ALD has been attempted, nickel is a versatile candidate with promising characteristics and important applications. In nanoscale devices, growth of nickel can be the first step toward synthesis of NiSi, an increasingly popular contact material.<sup>17,18</sup>

**Received:** April 21, 2017

**Accepted:** July 3, 2017

**Published:** July 3, 2017

Nickel is also a promising candidate for solar thermal technologies.<sup>5,19</sup> Nickel also has widespread applications in high-density magnetic recording media<sup>20,21</sup> and as an effective precursor for growth of carbon nanotubes.<sup>9,22</sup> Although there are a few reports on the growth of nickel by atomic layer deposition,<sup>17,18,23–25</sup> after a review of the literature one can conclude that there is a lot yet to be investigated about plasma-enhanced ALD of nickel thin films.

In addition to the fact that there are some important contradicting reports in the previously mentioned publications that necessitate more in-depth and thorough studies, several aspects of the subject have not been investigated yet. To the best of our knowledge, no substrate other than Si(100) has been tested for nickel ALD; no analytical research on substrate/film crystallographic orientation relationship has been conducted; and there are very few reports on the growth mechanics of nickel thin films using this method. This work introduces a new setup for deposition of nickel on sapphire, begins to address some of the aforementioned shortcomings, and aims to provide a better understanding of PEALD of nickel and metallic thin films in general.

## 2. EXPERIMENTAL SECTION

Depositions were carried out on sapphire, using a plasma-enhanced atomic layer deposition research system from Kurt J. Lesker (ALD-150 LX). A liquid organometallic compound, bis(ethylcyclopentadienyl)-nickel ( $\text{Ni}(\text{EtCP})_2$ ), provided by Strem Chemicals was used in conjunction with a  $\text{N}_2/\text{H}_2$  plasma as precursors. The organometallic was heated at 85 °C in order to provide the required vapor pressure. It is noteworthy that previous attempts by the authors to accomplish the deposition of metallic nickel using powder precursors had been unsuccessful, due to technical issues, related to the precursor delivery process.

After several attempts at various pulse widths, it was observed that the growth rate reached a plateau at 5 and 15 s for the precursor and forming gas, respectively. These values were therefore used for all the samples reported in this study. The purge times for both precursors were fixed at 7 s, and argon gas was used for this purpose. Five different samples were deposited at various substrate temperatures. The codenames used to refer to these samples, along with the effective substrate temperatures, are summarized in Table 1. All the samples

**Table 1. Summary of the Effective Values of Substrate Temperature for Different Samples<sup>a</sup>**

sample codename	effective substrate temperature
Ni-200	200 °C
Ni-250	250 °C
Ni-300	300 °C
Ni-350	320 °C
Ni-400	360 °C

<sup>a</sup>According to the manufacturer, the effective substrate temperature deviates from the set value at higher set temperatures.

were deposited on C-plane sapphire substrates, which were cleaned by a 60 s exposure to the  $\text{N}_2/\text{H}_2$  (19/1 ratio) plasma, immediately prior to the start of the deposition. All the structural and compositional characterizations were performed on films with the thickness of 20 nm.

The growth rate was monitored during deposition using an in situ fixed-angle spectroscopic ellipsometer (J. A. Woollam M2000DI) at the wavelength range of 300–1100 nm. The optical properties of the samples were investigated post deposition via a J. A. Woollam variable-angle spectroscopic ellipsometer, at incident angles 55°, 65°, and 75°. These measurements were carried out at room temperature. CompleteEASE software was used for analysis of all ellipsometry data. A Lucas Laboratories 4-point probe coupled with a Keithley

Source Measure Unit (model 2400) was used to study the resistivity of the films.

The surface profiles of the deposited samples were studied using a Veeco Dimension 3100 atomic force microscope (AFM). All the AFM images were captured using silicon tips provided by MikroMasch. Images were captured in tapping mode with the amplitude set point of 0.7 V. AFM data were analyzed with Nanoscope Analysis 1.5 software, to extract the surface roughness. In order to study the grain structure of the films, a Hitachi S-4800 field emission scanning electron microscope was utilized. The microscope was operated at 5 kV, using both secondary and backscattered electron signals. Only samples Ni-350 and Ni-400 had a sufficiently high electrical conductivity to avoid charge accumulation under SEM.

X-ray diffraction (XRD) was used to study the overall crystal structure of the films. A Bruker D8 Discover was used for this purpose. X-ray reflectometry (XRR) was also carried out using the same machine. The beam source was  $\text{Cu K}\alpha$ , and the tube was set to operate at 50 kV and 1000  $\mu\text{A}$ . 2D XRD frames were captured via a Vantec 500 detector. XRR data,  $\varphi$  scans, and  $\theta$ – $2\theta$  spectra were collected using a Bruker LINXEYE XE detector. All XRD and XRR data were analyzed in Bruker EVA and Bruker Leptos R software packages, respectively.

Transmission electron microscopy was used to study the structure of the films in greater detail. High-angle annular dark-field (HAADF) imaging and electron energy loss spectrum (EELS) imaging were performed simultaneously on a JEOL-2200FS scanning transmission electron microscope (STEM), operated at 200 kV. EELS spectrum imaging was obtained by scanning the electron beam with a nominal diameter of 0.5 nm along a line across the interface between different layers in the sample. The spectrum along the scanning line for each pixel was recorded and analyzed with Digital Micrograph software (Gatan Inc.). The signal extraction for each element from the spectrum image was performed by following the standard procedure of pre-edge background subtraction and integration on the edge.<sup>26</sup> High-resolution transmission electron microscopy (HRTEM) images were recorded on a Hitachi H9500 environmental TEM operated at 300 kV and analyzed with Digital Micrograph software (Gatan Inc.).

Sample preparation for TEM was performed using the two following steps: (1) A protective chromium layer was deposited using a JUV electron beam evaporation system, before deposition of  $\sim 1.8 \mu\text{m}$  of a protective platinum layer, followed by trench excavation from three sides, to produce a lamella with the thickness of  $\sim 1.5 \mu\text{m}$ . This step was carried out on a Zeiss NVision 40 focused ion beam (FIB) apparatus, using a 30 kV Ga ion beam. (2) Plucking and mounting of the lamella onto a copper TEM grid was followed by the thinning of the lamella to transparency ( $\sim 100 \text{ nm}$  thickness), which was performed on a Hitachi NB5000 FIB machine, using a 40 kV Ga ion beam.

## 3. RESULTS AND DISCUSSION

**3.1. Physical Properties.** The electrical resistivity of the samples is discussed first in order to identify the ones that exhibit a metallic behavior and rule out the unsuccessful depositions. As seen in Figure 1, the values of electrical resistivity show a sharp drop, as the growth temperature increases. Up until 320 °C (Ni-350), the resistivity is too high for the films to be considered metallic. Taking the temperature further up to 360 °C (Ni-400) does not have a considerable effect on the resistivity. It is noteworthy to mention that, although the thickness of any thin film is known to affect the physical properties, the final thickness of the samples under study ranged from 16 nm for the sample Ni-200 to 20 nm for Ni-400. Since these variations are negligible, in comparison with the changes in the resistivity, the effect of film thickness on resistivity can be ignored.

It is notable that the values observed at these temperatures, i.e.,  $\rho = 200\text{--}260 \mu\Omega\text{-cm}$ , are still about an order of magnitude higher than the resistivity of FCC nickel thin films of



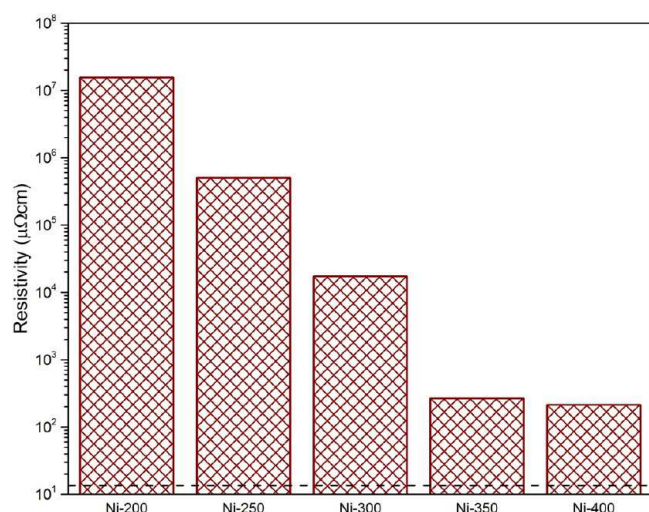


**Figure 1.** Values of electrical resistivity of the films; the dashed line indicates the resistivity of bulk FCC nickel.

comparable thickness, deposited via conventional methods like ion beam sputtering and electron beam evaporation.<sup>27</sup> A number of compositional and structural factors, such as film thickness,<sup>11</sup> impurities, and strain,<sup>27,28</sup> are known to considerably affect conductivity. These factors will be studied later on, in Sections 3.2–3.4.

Spectroscopic ellipsometry (SE) was employed to investigate the optical properties of the films. While fixed-angle in situ SE was used to study the growth rate of the films, the optical constants were extracted using postdeposition variable-angle SE at room temperature. For this aim, data were collected and analyzed in a wavelength range of 300–1100 nm. The Tauc–Lorentz dispersion function was used to describe the optical behavior of the sapphire substrate.

The b-spline layer parametrization method was selected to extract the optical constants of the nickel films. In this method, the optical constants are specified for a series of equally spaced nodes with predefined differences in photon energy. The b-spline recursive formula is then used to define a basis polynomial function at each point.<sup>29</sup> The summation of these functions yields the final curve. While using this method simplifies the mathematical fitting process by reducing the number of fitting parameters, it also maintains Kramers–Kronig consistency, rendering the resulting dispersion spectra physically correct.<sup>29</sup> This parametrization method has been successfully employed to describe the optical properties of various metallic thin films.<sup>30</sup>

The surface roughness measured through AFM was taken into account, as an input parameter for obtaining the best fit. The measured and modeled values of psi and delta for three different beam angles are displayed and compared in Figure 2. It is evident that a desirable match exists between the two, in this wavelength range. The extracted values of refractive index and extinction coefficient for the samples are plotted in Figure 3. In both cases the behavior of the optical constants gets closer to that of the pure bulk FCC nickel, with increasing growth temperature up until 320 °C (Ni-350), but no noticeable improvement is observed afterward. This is similar to the pattern observed in the case of resistivity, as discussed earlier. In light of these results, the discussion and analysis will be mainly focused on the samples Ni-350 and Ni-400. As other samples do not meet the desired requirements, they will only

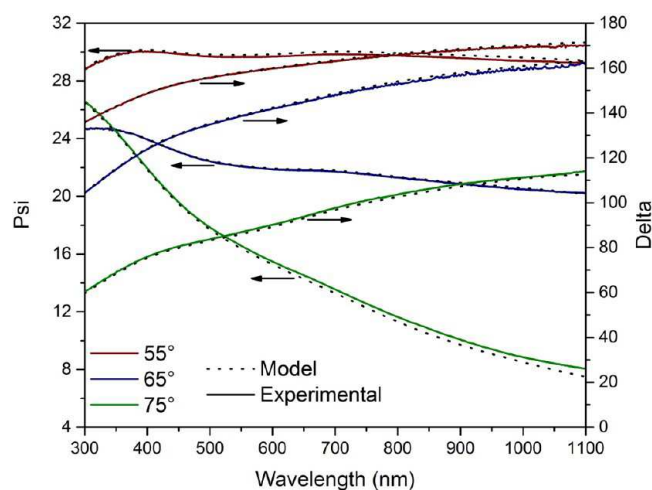


**Figure 2.** Comparison of the experimental and modeled psi and delta values for the sample Ni-400; data were collected and compared at three different beam incident angles.

be discussed when a meaningful trend is observed, whose discussion is deemed insightful.

**3.2. Compositional Analysis.** Electron energy loss spectrum imaging was employed to assess the level of impurities in the films. Since there is a substantial chance of contamination during thin-film growth, the level of impurities in the substrate was generally regarded as a baseline, as the chemical purity of the substrate is indisputable. In other words, there is a good chance of deposition-induced impurity in the nickel thin film, if the intensity of the signal associated with that impurity rises, when the substrate/film interface is crossed.

Figure 4 shows an annular dark field (ADF) image of the cross-section of sample Ni-400. The substrate, the nickel film, and the chromium protective layer have been labeled on the image. Two separate line scans were taken along the intersection, so that they cover the cross-section of the nickel film, as well as parts of the substrate and the protective chromium layer. One scan covered the low-energy loss end range of the spectrum, while the second one spanned over a higher-energy loss range. It is important to note that line marked on the image is merely a visual aid. The two sets of spectra result from separate scans across the interface, and the start and end points of the scan line are arbitrary. Therefore, they should be analyzed individually, not collectively.

The elemental line profiles are plotted in Figure 4b,c. Figure 4b shows the variation of the normalized integrated intensity of  $M_{2,3}$ ,  $L_{2,3}$ , and K edges for Ni, Al, and C signals, respectively, as a function of distance across the interface. As seen in Figure 4b, at around 20 nm the Al signal drops, and the Ni signal rises. This signifies the sapphire/Ni interface. The diffuseness of this area must be due to the proximity of Ni  $M_{2,3}$  and Al  $L_{2,3}$  edges,<sup>31</sup> which causes some overlap and inevitable intermixing of the integrated signals. At around 40 nm, the Ni signal drops. This marks the Ni/Cr interface. As observed, the carbon signal is prominent in the substrate, and it drops sharply, across the sapphire/Ni interface. The fact that carbon is mainly present in the chemically pure substrate and that its signal intensity drops afterward indicates that the detection of this signal is most probably due to postdeposition sample preparation steps, rather than ALD film growth. In the case of the latter, the change in carbon signal intensity across the interface would be reversed.

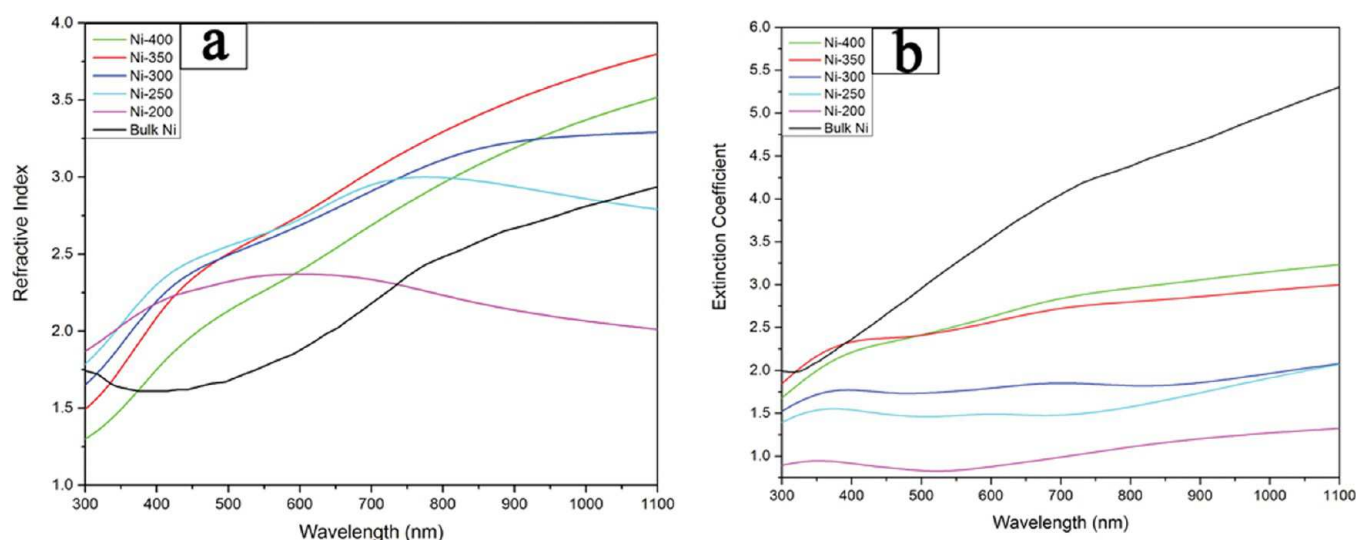


**Figure 3.** Variations of extinction coefficient (a) and refractive index (b) for various samples.

Figure 4c shows a second line scan across the interface. This scan spans over the  $L_{2,3}$  edge of nickel, as well as the K edge of oxygen and  $L_{2,3}$  edge of chromium. In this plot, a sharp drop in the O signal intensity is observed, which marks the end of the sapphire layer. The intensity then reaches zero, while the nickel signal is detected, and its intensity increases at the onset of the chromium layer. The interpretation is that there is no oxygen impurity in the nickel layer, as opposed to the protective chromium layer. The major conclusion from the EELS analysis is that there is no significant amount of carbon or oxygen in the ALD Ni films. This rules out the role of impurities in the noticeable disparity between the optoelectronic properties of the films and those of the bulk nickel.

**3.3. Structural Analysis.** Atomic force microscopy was used to measure the surface roughness of the films, whose value was then used for more accurate analysis of the spectroscopic ellipsometry and X-ray reflectometry data. For the sample Ni-400, the arithmetic average ( $R_a$ ) and root-mean-square ( $R_q$ ) values of surface roughness were determined to be 1.5 and 2.1 nm, respectively. A software-generated three-dimensional profile of the surface of sample Ni-400 is shown in Figure 5, along with a representative line scan, provided to better elucidate the variations of surface height. Although the general topography of the film resembles those of films with columnar structures,<sup>32–34</sup> considering the metallic conductivity of samples Ni-350 and Ni-400, scanning electron microscopy can be employed to provide a clearer view of their grain structure. The results are displayed in Figure 6. The granular structure of the films is distinctly noticeable in these images. Comparison of Figures 6a and 6b indicates that increasing growth temperature leads to a larger grain size. An image with a higher magnification is shown in Figure 6c. As seen, a good level of interconnection is observed among the adjacent grains. This is an indicator of a cohesive film growth. Similar observations have shown how an improved connectedness of grains occurs concurrently with improved physical properties.<sup>35</sup>

An in situ spectroscopic ellipsometry apparatus was used to study the variations of the growth rate during deposition. For this aim, a separate variable-angle spectroscopic ellipsometry machine was utilized for ex situ postdeposition assessment of optical constants, as discussed in Section 3.1. The output was then used in conjunction with the final thickness, determined

through cross-sectional TEM, and surface roughness, measured via AFM, to dynamically fit optical constants and thickness from the starting point to the end of the deposition.

The results plotted in the form of a thickness–cycles graph is shown in Figure 7. It can be seen that a stable growth rate is only achieved after about 12 cycles, after which the growth rate stabilizes at  $0.48 \text{ Å s}^{-1}$ . Since a stable linear growth is observed in the second stage, it is logical to conclude that a full coverage of the substrate has not been realized until the end of the first stage. On the other hand, if the first stage was solely spent on covering a monolayer on the substrate, the growth plot would be linear and with a lower slope than that of the second phase. However, the fact that a gradual and consistent increase in growth rate is observed can be suitably explained through a 3D island growth regime, hence the term nucleation phase. After the full coverage of the substrate is achieved, the growth regime switches to a mainly layer-by-layer growth, in which the growth is stable and changes linearly with respect to the deposition time. This stability might be indicative of an energetically coherent atomic structure of the growth front. This speculation is examined through a crystal structure analysis, as discussed in Section 3.4.

X-ray reflectometry was employed to assess the density of the films. For this purpose, the film thickness and roughness were taken as known parameters. Thickness, which affects the distance between consecutive maxima, was measured using a number of ADF images, similar to the one displayed in Figure 4. Roughness, which determines the attenuations rate of the intensity oscillations, was measured using AFM. These data were then used as input parameters to generate the simulated X-ray interference reflectivity patterns, known as Kiessig fringes. The simulation was done using a Bruker Leptos R software package. The Kiessig fringes for the sample Ni-400 are plotted and compared with a software-generated plot, as shown in Figure S1 (Supporting Information). In a typical XRR interference pattern for a single-layer film, the distance between adjacent signal peaks determines film thickness, and mass density and roughness mainly affect the oscillation amplitude and the mean intensity attenuation rate.<sup>36</sup> Using the above-mentioned parameters, the mass density of the nickel layer was found to be  $6.9 \text{ g/cm}^3$ . Interestingly, this is relatively close to the value of  $7.3 \text{ g/cm}^3$ , reported for hexagonal nickel (PDF #

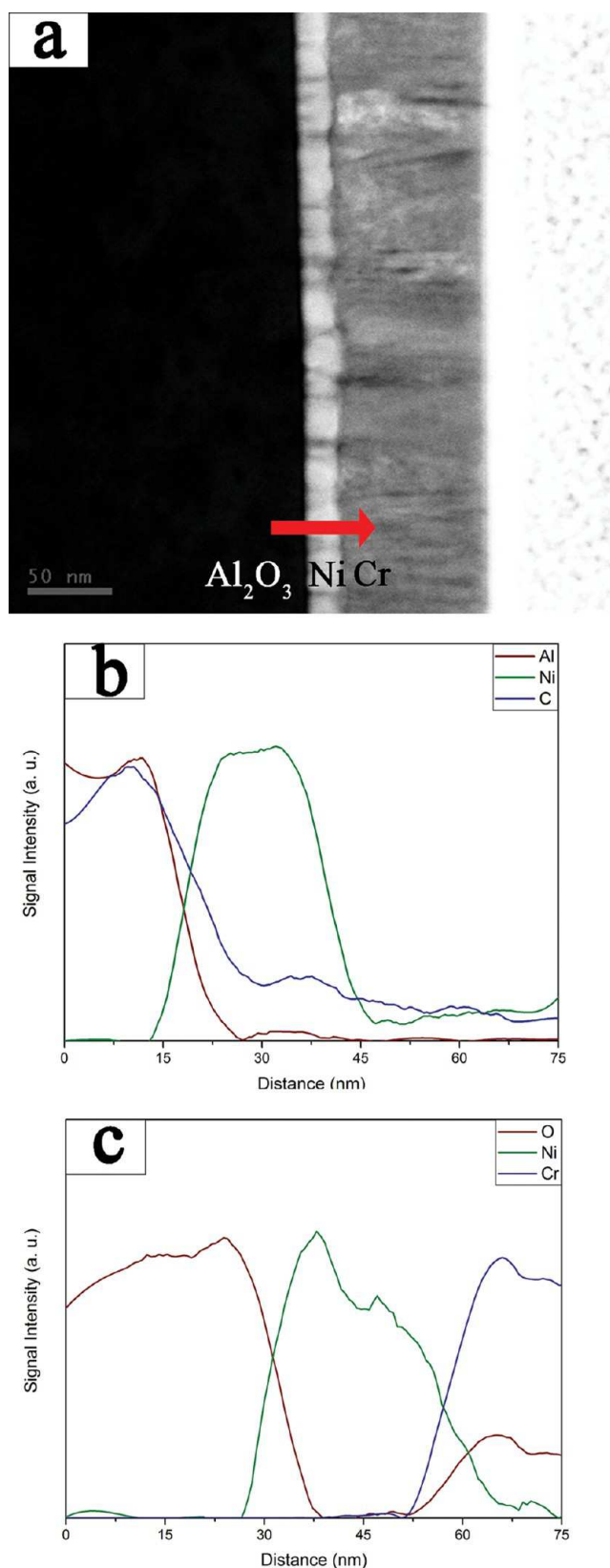


**Figure 4.** (a) Annular dark-field image of the cross-section of sample Ni-400, featuring the nickel film, capped between the sapphire substrate and the protective chromium layer. (b) Normalized integrated EELS intensities of Ni  $M_{2,3}$ , Al  $L_{2,3}$ , and C K edges. (c) Normalized integrated EELS intensities of Ni  $L_{2,3}$ , O K, and Cr  $L_{2,3}$  edges.

04-002-8298<sup>37</sup>). This proximity necessitates a comprehensive analysis of the crystal structure.

**3.4. Crystallographic Analysis.** Plots of coupled  $\theta$ – $2\theta$  scans of the samples deposited at various temperatures are shown in Figure 8. As seen, lower temperatures lead to amorphous samples. As the growth temperature increases, a spectrum forms which features three peaks at  $39.1^\circ$ ,  $41.8^\circ$ , and  $44.5^\circ$ . These peaks closely match those reported in PDF # 04-002-8298,<sup>37</sup> which describes the crystal structure of hexagonal nickel. Hexagonal nickel, with space group  $P6_3/mmc$ , is a metastable phase, whose formation requires special circumstances. One method of synthesizing hexagonal nickel thin films is through substrate-induced stabilization, as reported by Tian et al.<sup>38</sup> for the case of nickel thin films on MgO substrate.

In other words, what may give rise to a metastable phase in this case is a crystallographic relationship between the film and the substrate. At high deposition temperatures, such as those typically used in MBE and CVD, the kinetic energy of the atoms is high enough to provide the required mobility for dynamic rearrangement of atoms into the most stable form. In contrast, at low growth temperature, the crystal structure imposed by the substrate on the first atomic layers may be sustained and carried forward to the next layers.<sup>39</sup>

A possible substrate–film crystallographic relationship will result in preferential orientation of certain crystallographic planes in nickel grains. The quickest approach to examine such a condition is two-dimensional X-ray diffraction. A 2D-XRD frame of the sample Ni-400 is shown in Figure 9. In a 2D-XRD frame, diffraction from any crystal plane with a random orientation will appear in the form of an arc. On the contrary, those planes that make a constant angle with a vector normal to the substrate appear in the form of a dot.<sup>12</sup> Therefore, the relative diffuseness of the diffraction intensity in a 2D-XRD frame represents the relative degree of crystallographic misorientation for a given plane.

As seen in Figure 9, the reflection intensity of the (002) plane of the nickel film is concentrated around angles of  $\psi = 90^\circ$ . This means that hexagonal unit cells of nickel have a tendency to grow in such a way that aligns their  $c$ -axes relatively parallel with the normal to nickel/sapphire interface. The (101) planes, on the other hand, exhibit no sign of preferential orientation, as demonstrated in relatively uniform distribution of diffraction intensity along the arc at  $2\theta = 44.5^\circ$ . This suggests the grains have random in-plane orientation.

The out-of-plane misorientation can be probed through a phi scan (Figure S2 (Supporting Information)). Here, the X-ray source and the detector were kept at a symmetrical geometry with  $\omega$  (the angle between the beam and the surface) equal to  $20.8^\circ$ . With the Bragg condition satisfied for the diffraction of (002) planes, the sample was rotated  $360^\circ$  around the normal. In such a condition, small inevitable misalignment between the normal to sample surface and the vector that bisects incoming and reflected beams gives rise to two strong peaks,  $180^\circ$  apart in  $\phi$ , provided the reflecting planes are parallel to the surface. Observation of these two peaks is therefore considered an indication of preferential orientation of crystals.

High-resolution transmission electron microscopy was employed to more closely investigate the nickel/sapphire interface (Figure 10). Among the images taken, two distinct groups of lattice fringes were observed, representing different crystallographic planes of the nickel lattice. As seen in Figure 10, when the lattice fringes are parallel to the interface, they have an interplanar spacing of 0.207 nm. This value of  $d$ -



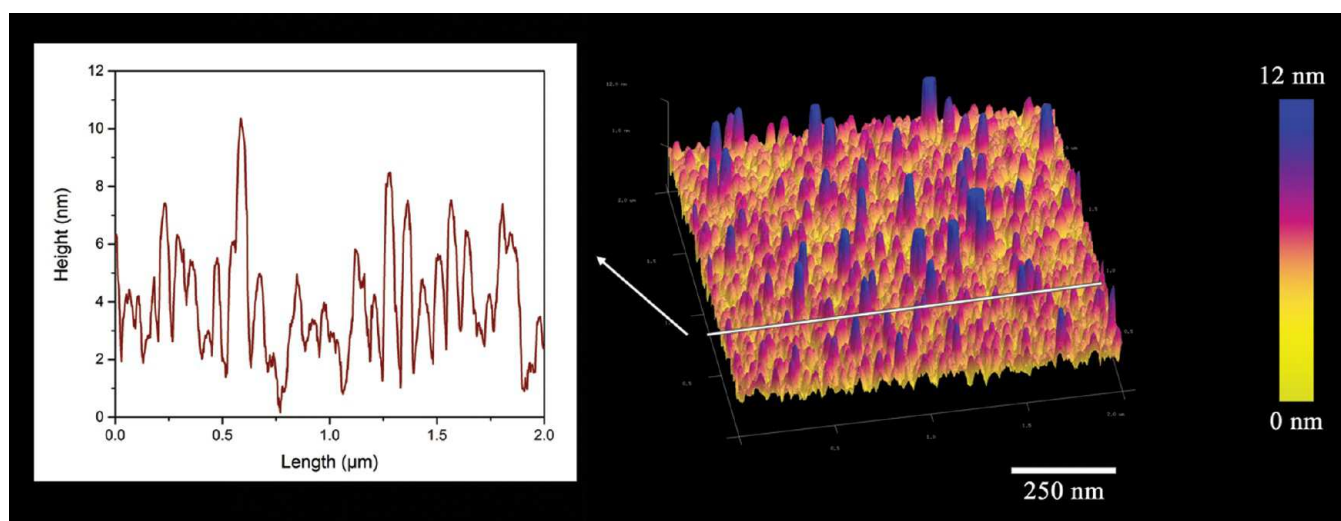


**Figure 5.** Three-dimensional reconstruction of the surface profile of sample Ni-400, along with a representative line scan; data collected using a scanning probe microscope in tapping mode.

spacing is close to the (002) interplanar spacing, as reported in PDF 04-002-8298.<sup>37</sup> Those grains with their (002) planes parallel to the interface obviously feature a clear crystallographic orientation relationship between the film and the substrate, i.e.,  $[001]_{\text{Ni}} \parallel [001]_{\text{sapphire}}$ .

The other group of planes was observed to be positioned such that their normals were at angles of 25–30° with the normal to the interface. These planes were spaced 0.220 nm apart. This is close to (101) interplanar spacing. In a hexagonal close-packed crystal structure (space group 194), the theoretical angle between normals to (002) and (101) planes can be calculated as  $\sim 28^\circ$ . One can therefore expect (001) planes of these grains to be also positioned parallel to the interface. However, random in-plane orientation of the planes means different zone axes for different grains. Therefore, different sets of lattice fringes will be observed for different grains. It must be noted that the finite number of HRTEM images means that this method should not be taken as a standalone solution to determine the grain orientation. When combined with more representative methods like 2D-XRD, however, HRTEM can be a good complementary analysis tool. The crystallographic analyses described here provide a clearer view of the structure of the films. The nickel films deposited at higher temperatures have a columnar structure, as seen in ADF and AFM images. The grains have a specific texture; i.e., their [001] crystallographic directions are parallel to the normal to the interface.

The relatively low density of the films suggests that the films are under tensile strain. The theoretical equilibrium lattice constants for bulk hcp nickel can be calculated as  $a = 2.50 \text{ \AA}$  and  $c = 4.08 \text{ \AA}$ .<sup>40</sup> These numbers lead to a theoretical mass density of  $8.52 \text{ g/cm}^3$  for bulk hcp nickel. On the other hand, it is well-known that on the (001) plane of sapphire the oxygen atoms form a two-dimensional hexagonal lattice, whose primary axes are rotated by 30°, with respect to those of the sapphire lattice.<sup>41</sup> This has been the basis for epitaxial growth of III–N materials on sapphire, in which case the effective lattice parameter of sapphire can be regarded as  $a^* = 2.75 \text{ \AA}$ , instead of the regular value of  $a = 4.76 \text{ \AA}$ .<sup>12,42</sup> Applying simple crystallographic calculations to the results of HRTEM measurements of  $d$ -spacings (Figure 10), one can derive the lattice constants of the hexagonal nickel film (sample Ni-400) to be  $a$

$= 2.71 \text{ \AA}$  and  $c = 4.42 \text{ \AA}$ . The strong deviation of the lattice constant “ $a$ ” from the equilibrium value of  $2.50 \text{ \AA}$  and its proximity to sapphire’s  $a^* = 2.75 \text{ \AA}$  is in line with the conclusions taken from XRD and HRTEM analyses regarding the crystallographic relationship between the film and the substrate. Furthermore, the derived values for the lattice constants result in a calculated mass density of  $6.82 \text{ g/cm}^3$ , which is very close to the experimental value of  $6.9 \text{ g/cm}^3$ , as measured via XRR (Section 3.3).

Comparing the equilibrium and the measured lattice constants, one can estimate that the films are under  $\sim 8.5\%$  tensile strain. Considering the fact that the films have a low concentration of impurities, the tensile strain is likely to be the main cause of the high resistivity of the films. It must be noted that an increase in resistivity by an order of magnitude as a result of tensile strains of  $\sim 6\%$  has been reported for metallic thin films.<sup>28</sup> Further analysis to determine the exact state of the stress and its effect on the electrical resistivity may be conducted by the authors in the future, but it is beyond the scope of this publication.

In summary, the films show a good crystallographic relationship with the sapphire substrate, and the method described in this publication is a reliable alternative to the conventional thin-film deposition methods, such as sputtering and CVD. The true value of this research can be better realized when one considers one of the inherent advantages of ALD films, which is their conformality or their ability to grow on three-dimensional surfaces with a consistent thickness. Taking advantage of this capability, this group has recently developed the technology for ceramic foams coated with carbon nanotubes using conformal nickel films as catalysts. The preliminary results of this research have been recently published.<sup>9</sup> It was observed that the basics of nickel thin-film deposition using plasma-enhanced ALD are transferable from the sapphire substrate to aluminum oxide foams. In addition to this particular application, the ability to deposit pure metallic thin films has several applications in metallization,<sup>43,44</sup> solar cell cathodes,<sup>45</sup> and solid oxide fuel cells,<sup>46</sup> among others.

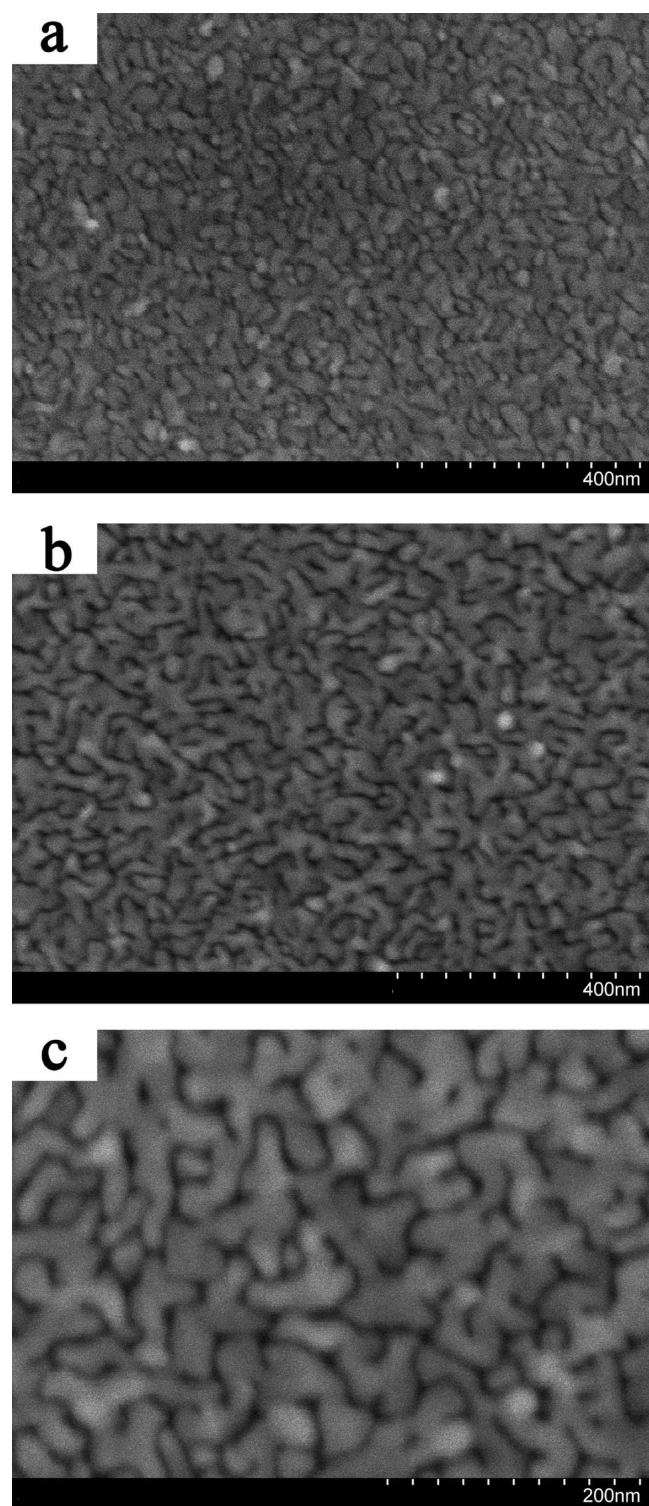


**Figure 6.** Top-view scanning electron microscopy images of samples Ni-350 (a) and Ni-400 (b,c).

#### 4. CONCLUSION

Metastable HCP nickel thin films were deposited at various growth temperatures, using plasma-enhanced atomic layer deposition. Substrate temperatures of 320 °C and above were needed for the deposition of metallic films. The films were void of carbon and oxygen impurities. Differences were observed between the physical properties of the films and those of the bulk FCC nickel. The mass density of the films deposited at

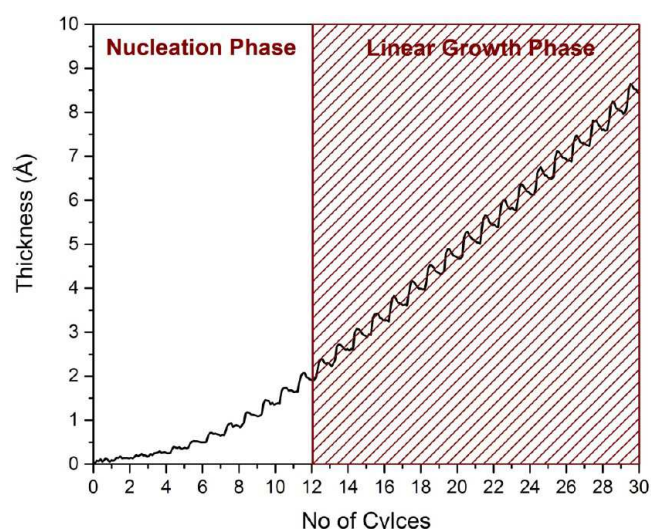


**Figure 7.** Variations of thickness as a function of number of ALD cycles for the sample Ni-400; the two stages of nucleation and growth are marked on the graph.

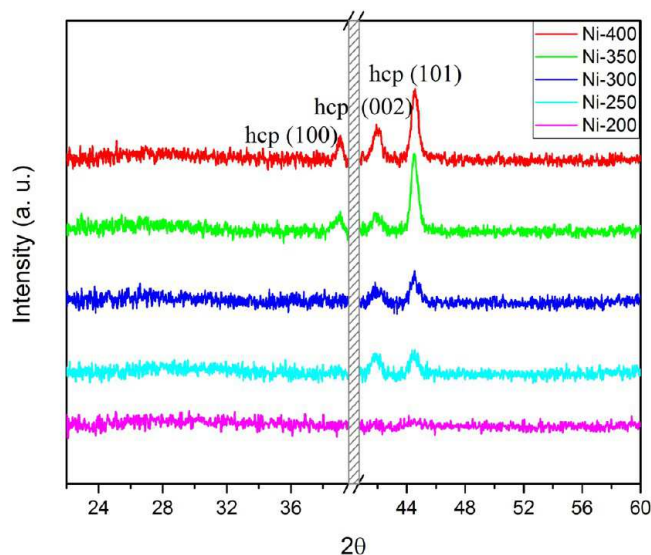


**Figure 8.**  $\theta$ -2 $\theta$  X-ray diffraction spectra for different samples; the three crystallographic planes of hcp nickel with the highest diffraction intensity are marked on the graphs.

360 °C was found to be ~20% lower than the bulk value, and the films were found to have grown under tensile strain. AFM and SEM observations verified a granular structure for the films. All of the films featured a close-packed hexagonal structure. Two-dimensional X-ray diffraction analysis of the structure showed a strong crystallographic relationship between the films and the sapphire substrate ( $[001]_{\text{Ni}} \parallel [001]_{\text{sapphire}}$ ). Overall, the films featured a strong crystallographic order along the normal to the film/substrate interface. The in-plane orientation, however, did not follow a specific pattern. The HRTEM observations also corroborated the XRD conclusions. In summary, the combination of the deposition parameters used in this study proved to constitute a successful method for growth of high quality hexagonal nickel thin films. This method can be employed for any application requiring conformal growth of nickel thin films on three-dimensional structures.



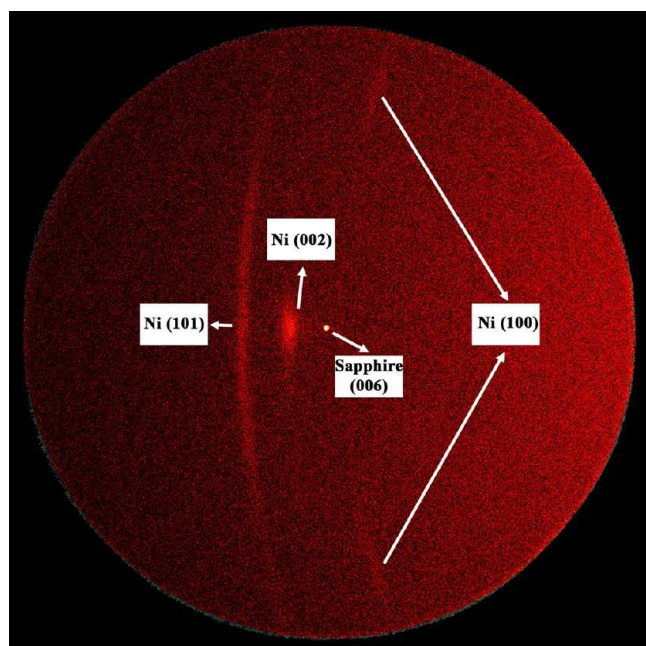


**Figure 9.** Two-dimensional diffraction frame, on which arcs and dots representing various crystallographic planes of sapphire and nickel are marked.

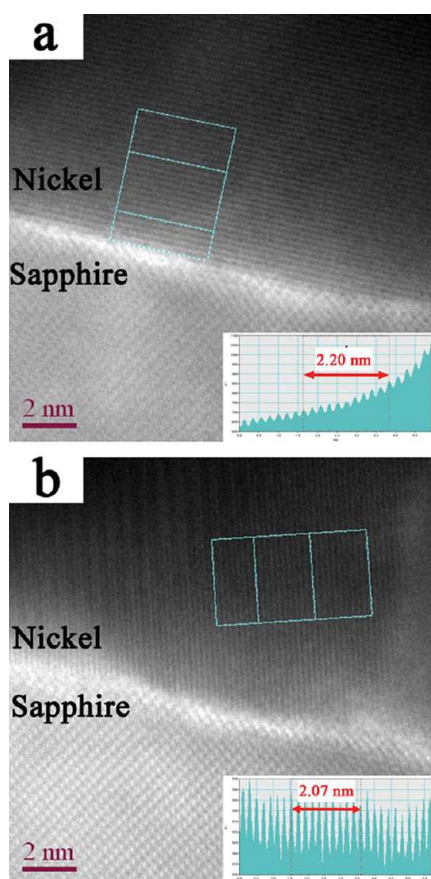


**Figure 10.** High-resolution transmission electron micrographs of two different grains of nickel; basic image analyses featuring the interplanar spacing of each set of crystallographic planes are superimposed on each image. The interplanar spacings are close to those of (002) planes (a) and (101) planes (b) in the hexagonal nickel lattice.

## ■ ASSOCIATED CONTENT

### Supporting Information

The Supporting Information is available free of charge on the ACS Publications website at DOI: 10.1021/acsami.7b05571.

X-ray reflectometry curves and azimuthal X-ray diffraction scans of sample Ni-400 (PDF)

## ■ AUTHOR INFORMATION

### Corresponding Author

\*E-mail: [p.motamedi@ualberta.ca](mailto:p.motamedi@ualberta.ca).

### ORCID

Pouyan Motamedi: 0000-0003-0345-8239

### Notes

The authors declare no competing financial interest.

## ■ ACKNOWLEDGMENTS

The authors would like to express their gratitude for the help received from the following individuals: Dr. Triratna Muneshwar for his valuable help with atomic layer deposition, Dr. Douglas Vick for his help with the preparation of the TEM samples, and Mr. Steve Launspach for his valuable discussions regarding the XRD analysis. Funding for this work was provided by the Security Material Technologies Program (National Research Council Canada) and by Defense Research and Development Canada. The graphical abstract of this article was produced, in part, using Visualization for Electronics and Structural Analysis (Vesta) software.<sup>47</sup>

## ■ REFERENCES

- (1) Ghosh, D. S. Basics of Ultrathin Metal Films and Their Use as Transparent Electrodes. *Ultrathin Metal Transparent Electrodes for the Optoelectronics Industry* **2013**, 11–33.
- (2) Theuring, M.; Steenhoff, V.; Geißendörfer, S.; Vehse, M.; von Maydell, K.; Agert, C. Laser Perforated Ultrathin Metal Films for Transparent Electrode Applications. *Opt. Express* **2015**, 23, A254.
- (3) Zou, J.; Li, C.-Z.; Chang, C.-Y.; Yip, H.-L.; Jen, A. K.-Y. Interfacial Engineering of Ultrathin Metal Film Transparent Electrode for Flexible Organic Photovoltaic Cells. *Adv. Mater.* **2014**, 26, 3618–3623.
- (4) Liu, Y.; Guo, C.-F.; Huang, S.; Sun, T.; Wang, Y.; Ren, Z. A New Method for Fabricating Ultrathin Metal Films as Scratch-Resistant Flexible Transparent Electrodes. *J. Mater.* **2015**, 1, 52–59.
- (5) Ahmad, N.; Stokes, J.; Fox, N. A.; Teng, M.; Cryan, M. J. Ultra-Thin Metal Films for Enhanced Solar Absorption. *Nano Energy* **2012**, 1, 777–782.
- (6) Li, Z.; Rahtu, A.; Gordon, R. G. Atomic Layer Deposition of Ultrathin Copper Metal Films from a Liquid Copper(I) Amidinate Precursor. *J. Electrochem. Soc.* **2006**, 153, C787–C794.
- (7) Lorenz, R. M.; Kuyper, C. L.; Allen, P. B.; Lee, L. P.; Chiu, D. T. Direct Laser Writing on Electrolessly Deposited Thin Metal Films for Applications in Micro- and Nanofluidics. *Langmuir* **2004**, 20, 1833–1837.
- (8) Juskova, P.; Foret, F. Application of Thin Metal Film Elements in Bioanalysis. *J. Sep. Sci.* **2011**, 34, 2779–2789.
- (9) Bosnick, K.; Motamedi, P.; Patrie, T.; Cadien, K. Conformal Carbon Nanotube Coatings for Ceramic Composite Structures. *MRS Adv.* **2017**, 2, 1499–1503.
- (10) O'Connor, B.; Haughn, C.; An, K.-H.; Pipe, K. P.; Shtein, M. Transparent and Conductive Electrodes Based on Unpatterned, Thin Metal Films. *Appl. Phys. Lett.* **2008**, 93, 223304.
- (11) Lacy, F. Developing a Theoretical Relationship between Electrical Resistivity, Temperature, and Film Thickness for Conductors. *Nanoscale Res. Lett.* **2011**, 6, 636.
- (12) Motamedi, P.; Cadien, K. Structure–property Relationship and Interfacial Phenomena in GaN Grown on C-Plane Sapphire via

Plasma-Enhanced Atomic Layer Deposition. *RSC Adv.* **2015**, *5*, 57865–57874.

(13) Motamedi, P.; Cadien, K. Structural and Optical Characterization of Low-Temperature ALD Crystalline AlN. *J. Cryst. Growth* **2015**, *421*, 45–52.

(14) Motamedi, P.; Dalili, N.; Cadien, K. C. A Route to Low Temperature Growth of Single Crystal GaN on Sapphire. *J. Mater. Chem. C* **2015**, *3*, 7428–7436.

(15) Kim, H.; Oh, I. Review of Plasma-Enhanced Atomic Layer Deposition: Technical Enabler of Nanoscale Device Fabrication. *Jpn. J. Appl. Phys.* **2014**, *53*, 03DA01–1–7.

(16) Johnson, R. W.; Hultqvist, A.; Bent, S. F. A Brief Review of Atomic Layer Deposition: From Fundamentals to Applications. *Mater. Today* **2014**, *17*, 236–246.

(17) Kim, W.-H.; Lee, H.-B.-R.; Heo, K.; Lee, Y. K.; Chung, T.-M.; Kim, C. G.; Hong, S.; Heo, J.; Kim, H. Atomic Layer Deposition of Ni Thin Films and Application to Area-Selective Deposition. *J. Electrochem. Soc.* **2011**, *158*, D1–D5.

(18) Lee, H. B. R.; Bang, S. H.; Kim, W. H.; Gu, G. H.; Lee, Y. K.; Chung, T. M.; Kim, C. G.; Park, C. G.; Kim, H. Plasma-Enhanced Atomic Layer Deposition of Ni. *Jpn. J. Appl. Phys.* **2010**, *49*, 05FA11–4.

(19) Yin, Y.; Pan, Y.; Rubanov, S.; Bilek, M. M. M.; McKenzie, D. R. Sputtered Nanocrystalline Nickel Thin Films for Solar Thermal Energy Applications. *Nanosci. Nanotechnol. Lett.* **2009**, *1*, 32–36.

(20) Halano, A.; Li, C. C.; Chen, Q.; Chour, K.-W.; Li, X.; Rou, S. A. Nickel Based Alloy Layer for Perpendicular Recording Media. US 8,053,096 B2, 2011.

(21) Kumar, P. Magnetic Behavior of Surface Nanostructured 50-Nm Nickel Thin Films. *Nanoscale Res. Lett.* **2010**, *5*, 1596–1602.

(22) Tessonnier, J.-P.; Su, D. S. Recent Progress on the Growth Mechanism of Carbon Nanotubes: A Review. *ChemSusChem* **2011**, *4*, 824–847.

(23) Shimizu, H.; Sakoda, K.; Momose, T.; Koshi, M.; Shimogaki, Y. Hot-Wire-Assisted Atomic Layer Deposition of a High Quality Cobalt Film Using Cobaltocene: Elementary Reaction Analysis on NH<sub>x</sub> Radical Formation. *J. Vac. Sci. Technol., A* **2012**, *30*, 01A144.

(24) Yuan, G.; Shimizu, H.; Momose, T.; Shimogaki, Y. Kinetic Study on Hot-Wire-Assisted Atomic Layer Deposition of Nickel Thin Films. *J. Vac. Sci. Technol., A* **2014**, *32*, 01A104.

(25) Yuan, G.; Shimizu, H.; Momose, T.; Shimogaki, Y. Role of NH<sub>3</sub> Feeding Period to Realize High-Quality Nickel Films by Hot-Wire-Assisted Atomic Layer Deposition. *Microelectron. Eng.* **2014**, *120*, 230–234.

(26) Egerton, R. F. *Electron Energy-Loss Spectroscopy in the Electron Microscope*, 3rd ed.; Plenum Press, 2011.

(27) Johnson, B. C. Electrical Resistivity of Copper and Nickel Thin-Film Interconnections. *J. Appl. Phys.* **1990**, *67*, 3018–3024.

(28) Khan, M.; Islam, M.; Akram, A.; Qi, Z.; Li, L. Residual Strain and Electrical Resistivity Dependence of Molybdenum Films on DC Plasma Magnetron Sputtering Conditions. *Mater. Sci. Semicond. Process.* **2014**, *27*, 343–351.

(29) Johs, B.; Hale, J. S. Dielectric Function Representation by B-Splines. *Phys. Status Solidi A* **2008**, *205*, 715–719.

(30) Leick, N.; Weber, J. W.; Mackus, A. J. M.; Weber, M. J.; van de Sanden, M. C. M.; Kessels, W. M. M. *In Situ* Spectroscopic Ellipsometry during Atomic Layer Deposition of Pt, Ru and Pd. *J. Phys. D: Appl. Phys.* **2016**, *49*, 115504.

(31) Gatan EELS Atlas <http://www.eels.info/atlas> (accessed Feb 21, 2017).

(32) Cheemadan, S.; Rafiudeen, A.; et al. Highly Transparent Conducting CdO Thin Films by Radiofrequency Magnetron Sputtering for Optoelectronic Applications Highly Transparent Conducting CdO Thin Films by Radiofrequency Magnetron Sputtering for Optoelectronic Applications Saheer Cheemadan. *J. Nanophotonics* **2016**, *10*, 33007–13.

(33) Ukahapanyakul, P.; Gridsadanurak, N.; Sapcharoenkun, C.; Treetong, A.; Kasamechongchun, P.; Khemthong, P.; Horprathum, M.; Porntheeraphat, S.; Wongwiriyan, W.; Nukeaw, J.; Klamchuen,

A. Texture Orientation of Silver Thin Films Grown via Gas-Timing Radio Frequency Magnetron Sputtering and Their SERS Activity. *RSC Adv.* **2016**, *6*, 7661–7667.

(34) Zhao, F.; Franz, S.; Vincenzo, A.; Cavallotti, P. L. Nanopillar Array Film of Cellular Cobalt by Wet Etching of the Grain Boundaries. *Mater. Lett.* **2015**, *141*, 172–175.

(35) Park, J.; Jin, K.; Han, B.; Kim, M. J.; Jung, J.; Kim, J. J.; Lee, W. Atomic Layer Deposition of Copper Nitride Film and Its Application to Copper Seed Layer for Electrodeposition. *Thin Solid Films* **2014**, *556*, 434–439.

(36) Chason, E.; Mayer, T. M. Thin Film and Surface Characterization by Specular X-Ray Reflectivity. *Crit. Rev. Solid State Mater. Sci.* **1997**, *22*, 1–67.

(37) ICDD. *PDF-4+ 2015* (Database); Kabekkodu, S., Ed.; International Centre for Diffraction Data: Newtown Square, PA, USA, 2015.

(38) Tian, W.; Sun, H. P.; Pan, X. Q.; Yu, J. H.; Yeadon, M.; Boothroyd, C. B.; Feng, Y. P.; Lukaszew, R. A.; Clarke, R. Hexagonal Close-Packed Ni Nanostructures Grown on the (001) Surface of MgO. *Appl. Phys. Lett.* **2005**, *86*, 131915.

(39) Thompson, C. V. Grain Growth in Thin Films. *Annu. Rev. Mater. Sci.* **1990**, *20*, 245–268.

(40) Cheng, Z.; Zhu, J.; Tang, Z. Magnetism of Hexagonal Closed-Packed Ni Nanowires from Ab Initio Calculations. *J. Appl. Phys.* **2009**, *105*, 103906.

(41) Xue, M. Y. Effect of Sapphire Substrate Nitridation on the Elimination of Rotation Domains in ZnO Epitaxial Films. *J. Phys. D: Appl. Phys.* **2004**, *37*, 3424–3424.

(42) Bradshaw, M. L.; Lynn, M. Epitaxial Growth of Indium Nitride on (0001) Sapphire. ProQuest Diss. Theses; Thesis (Ph.D.), Arizona State Univ. 2009; Publ. Number AAI3357255; *Source Diss. Abstr. Int.*; Vol. 70–05, Sect. B, p 3118; 76 p. 2009.

(43) Li, W.-M. Recent Developments of Atomic Layer Deposition Processes for Metallization. *Chem. Vap. Deposition* **2013**, *19*, 82–103.

(44) Tripathi, T. S.; Karppinen, M. Efficient Process for Direct Atomic Layer Deposition of Metallic Cu Thin Films Based on an Organic Reductant. *Chem. Mater.* **2017**, *29*, 1230–1235.

(45) Kim, D. H.; Losego, M. D.; Peng, Q.; Parsons, G. N. Atomic Layer Deposition for Sensitized Solar Cells: Recent Progress and Prospects. *Adv. Mater. Interfaces* **2016**, *3*, 1–12.

(46) Jeong, H.; Kim, J. W.; Park, J.; An, J.; Lee, T.; Prinz, F. B.; Shim, J. H. Bimetallic Nickel/Ruthenium Catalysts Synthesized by Atomic Layer Deposition for Low-Temperature Direct Methanol Solid Oxide Fuel Cells. *ACS Appl. Mater. Interfaces* **2016**, *8*, 30090–30098.

(47) Momma, K.; Izumi, F. VESTA 3 for Three-Dimensional Visualization of Crystal, Volumetric and Morphology Data. *J. Appl. Crystallogr.* **2011**, *44*, 1272–1276.